Acceleration of the Primary Basic Functions Calculation from the EFIE-characteristic Basis Function Method (CBFM) Combined with a New Physical Optics Approximation

Christophe Bourlier

Machine Copy for Proofreading, Vol. x, y–z, 2023

Acceleration of the Primary Basic Functions Calculation from the EFIE-Characteristic Basis Function Method (CBFM) Combined with a New Physical Optics Approximation

Christophe Bourlier*

Abstract—This paper presents a new scheme to implement the iterative physical optics (IPO) approximation with edge diffraction for the scattering from large perfectly-conducting objects, for which, multiple reflection occurs. The use of the EFIE (electric field integral equation) discretized by the Galerkin MoM (method of moments) with Rao-Wilton-Glisson basis functions leads to solve a linear system. The characteristic basis function method (CBFM) needs to invert the self-impedance sub-matrices to calculate the primary basis functions (PBFs). To accelerate this stage, these sub-linear systems are directly solved from the physical optics (PO) approximation. In addition, to improve the precision of PO, the EFIE-PO self-impedance matrix is derived analytically. This avoids to apply the magnetic field integral equation (MFIE), for which its principal value is related to PO. Numerical results showed that the resulting algorithm, EFIE-CBFM-PO, predicts inherently the edge diffraction. A domain decomposition method is able to split up the geometry into blocks, for which either the PO or a LU decomposition is applied according the sub-geometry. To accelerate the coupling steps, the adaptive cross approximation (ACA) is also implemented and the resulting method is tested on different targets having a curvature and producing multiple reflections. The numerical results show that EFIE-CBFM-PO is more accurate than the conventional EFIE-CBFM-POJ (based on Jakobus et al. work), specially for objects with curvature.

1. INTRODUCTION

The method of moments (MoM) [1] has been commonly used to solve the electromagnetic scattering problems. It transforms integral equations into matrix equations. For a perfectly-conducting object, the EFIE (electric field integral equation) is commonly applied. To solve the matrix equations, iterative solvers can be employed, like the based-conjugate gradient algorithms [1, 2], the steepest descent fast multipole method [3–5] (SDFMM), the adaptive integral method (AIM) [6–10] and the sparse-matrix canonical grid (SMCG) [11–15]. Compared with the iterative solvers, the direct solvers have some attractive features. For example, they do not suffer from the unpredictable convergence and can efficiently solve the problems with multiple right-hand-side vectors. However, it is well known that the conventional direct solvers, such as lower-upper (LU) decomposition, are very expensive for large targets. To overcome this issue, efficient algorithms [16–20], based on subdivision of the entire geometry into several subdomains (blocks), have been developed to rigorously solve large problems. By this way, the solution is calculated from an iterative scheme, in which size smaller problems are solved from direct or iterative solvers. In this paper, one focuses on the characteristics basis function method (CBFM) [16, 21–25].

On the other hand, to handle very large problems (high frequency), the physical optics (PO) approximation can be applied. For canonical geometries, the scattered field can be analytically

Received 19 January 2023

* Corresponding author: Christophe Bourlier (christophe.bourlier@univ-nantes.fr).

The author is with Nantes Université, CNRS, IETR (Institut d'Électronique et des Technologies numéRiques), UMR 6164, F-44000 Nantes, France.

evaluated [26–31] by introducing special functions, especially in the near field and for complex shapes. For complex geometries, numerical techniques have also been developed [32–35], especially for different excitations [36, 37]. For concave object, it is necessary to evaluate the scattered field associated to the double bounce. It is then impossible to derive closed-form expressions even for canonical geometries, without the introduction of simplifying assumptions [38–45]. Other accelerations of PO were proposed in the context of open-ended cavities, for which multiple bounces occur, with the iterative PO (IPO) method [46–51]. In addition, the IPO can be improved [52] by adding the edge diffraction contribution from an equivalent current method [53, 54].

Classically, in the lit region, the PO contribution can be obtained from the principal value of the magnetic field integral equation (MFIE). The purpose of this paper is to address a new IPO numerical scheme based on the EFIE formulation, for which the PO impedance matrix is derived to calculate the primary basis functions (PBFs). For a perfectly-conducting surface, Jakobus et al. [55] expressed the surface currents on the edges from the PO approximation, named POJ. In [23], POJ is generalized to a dielectric (rough) surface, called the modified equivalent current approximation (MECA), to efficiently calculate the PBFs. By applying PO on each block, which evaluates the single-reflection contribution, the multiple bounces are accounted for by interacting the blocks between them. To expedite this stage, the adaptive cross approximation (ACA) [56, 57] is applied to compress the inter-blocks coupling matrices.

This paper will show that EFIE-CBFM-PO is more accurate than EFIE-CBFM-POJ, specially for objects with curvature. The use of EFIE-CBFM-POJ does not require to invert a matrix whereas EFIE-CBFM-PO needs this operation. To exploit the sparsity of the EFIE-PO impedance matrix, a basic iterative technique is also addressed (paragraph 4.6) to accelerate the calculation of the PBFs. In addition, to evaluate the gain in saving time, the theoretical and numerical complexities of the different hybridizations are presented (paragraph 4.7). This will show that the fact to use the MatLab software, the expected complexities can be overestimated when iterative solvers are included.

The paper is organized as follows. Section 2 addresses a brief review of CBFM combined with ACA and Section 3 details the derivation of the EFIE based-PO impedance matrix. Section 4 shows numerical results of the RCS for a plate (single bounce), a sphere (single bounce with curvature), a dihedral (at least two bounces), an open-ended cavity (multiple bounces) and a paraboloid. The last section gives concluding remarks.

2. CHARACTERISTIC BASIS FUNCTION METHOD (CBFM)

The EFIE is solved using the MoM to determine the field scattered by a perfectly-conducting object. The use of the Galerkin method with Rao-Wilton-Glisson basis functions [58] yields the linear system $\bar{\mathbf{Z}}\mathbf{a} = \mathbf{b}$ [1, 20]. The matrix $\bar{\mathbf{Z}}$ is the impedance matrix and $\mathbf{b}$ the source vector. The time convention $e^{-j\omega t}$ is used throughout this paper.

The first stage of CBFM [16, 59, 20] decomposes the geometry into P sub-geometries (blocks). The impedance matrix $\bar{\mathbf{Z}}$ takes the from

$$\begin{bmatrix} \bar{\mathbf{Z}}_{1,1} & \bar{\mathbf{Z}}_{1,2} & \dots & \bar{\mathbf{Z}}_{1,P} \\ \bar{\mathbf{Z}}_{2,1} & \bar{\mathbf{Z}}_{2,2} & \dots & \bar{\mathbf{Z}}_{2,P} \\ \vdots & \vdots & \ddots & \vdots \\ \bar{\mathbf{Z}}_{P,1} & \bar{\mathbf{Z}}_{P,2} & \dots & \bar{\mathbf{Z}}_{P,P} \end{bmatrix} \begin{bmatrix} \mathbf{a}_1 \\ \mathbf{a}_2 \\ \vdots \\ \mathbf{a}_P \end{bmatrix} = \begin{bmatrix} \mathbf{b}_1 \\ \mathbf{b}_2 \\ \vdots \\ \mathbf{b}_P \end{bmatrix}, \tag{1}$$

where $\bar{\mathbf{Z}}_{p,p}$ are the self-impedance matrix of the block number p and $\bar{\mathbf{Z}}_{p_1,p_2}$ the coupling-impedance matrix between the blocks p_1 and p_2. $\mathbf{a}_p$ and $\mathbf{b}_p$ are sub-vectors of the block p.

For each block, the second stage calculates the primary basis function (PBFs) by solving the matrix equation [59]

$$\bar{\mathbf{Z}}_{i',i'}\mathbf{Y}_{i',k_{\mathrm{IPW}}} = \mathbf{B}_{i',k_{\mathrm{IPW}}}. \tag{2}$$

The symbol prime in the subscript of Equation (2) shows that the block is enlarged of some n_{OL} adjacent edges. This overlapping improves the accuracy of CBFM. The linear system (2) is solved by considering $2N_{\mathrm{IPW},i}$ bi-polarized incident plane waves $\{\mathbf{B}_{i',k_{\mathrm{IPW}}}\}$ ($k_{\mathrm{IPW}} \in [1; 2N_{\mathrm{IPW},i}]$). The vectors $\{\mathbf{Y}_{i',k_{\mathrm{IPW}}}\}$ are stored in a matrix $\bar{\mathbf{J}}_i$ of size $N_{\mathrm{Edge},i} \times 2N_{\mathrm{IPW},i}$, where $N_{\mathrm{Edge},i}$ is the number of edges of the block i

without overlapping (the overlapped edges of $\mathbf{Y}_{i',k_{\mathrm{IPW}}}$ are removed). The integer $N_{\mathrm{IPW},i}$ has not to be too large so that the matrix size is moderate. Thus, a singular value decomposition (SVD) filtering with threshold ϵ_{CBFM} is applied in order to avoid linear dependency. As a consequence, the size of $\bar{\mathbf{J}}_i$ becomes $N_{\mathrm{Edge},i} \times N_{\mathrm{IPW,SVD},i}$ with $N_{\mathrm{IPW,SVD},i} < 2N_{\mathrm{IPW},i}$.

The last stage of CBFM solves a reduced linear system $\bar{\mathbf{Z}}^{\mathrm{R}}\mathbf{a}^{\mathrm{R}} = \mathbf{b}^{\mathrm{R}}$ defined as

$$\begin{bmatrix} \bar{\mathbf{Z}}^{\mathrm{R}}_{1,1} & \bar{\mathbf{Z}}^{\mathrm{R}}_{1,2} & \dots & \bar{\mathbf{Z}}^{\mathrm{R}}_{1,P} \\ \bar{\mathbf{Z}}^{\mathrm{R}}_{2,1} & \bar{\mathbf{Z}}^{\mathrm{R}}_{2,2} & \dots & \bar{\mathbf{Z}}^{\mathrm{R}}_{2,P} \\ \vdots & \vdots & \ddots & \vdots \\ \bar{\mathbf{Z}}^{\mathrm{R}}_{P,1} & \bar{\mathbf{Z}}^{\mathrm{R}}_{P,2} & \dots & \bar{\mathbf{Z}}^{\mathrm{R}}_{P,P} \end{bmatrix} \begin{bmatrix} \mathbf{a}^{\mathrm{R}}_1 \\ \mathbf{a}^{\mathrm{R}}_2 \\ \vdots \\ \mathbf{a}^{\mathrm{R}}_P \end{bmatrix} = \begin{bmatrix} \mathbf{b}^{\mathrm{R}}_1 \\ \mathbf{b}^{\mathrm{R}}_2 \\ \vdots \\ \mathbf{b}^{\mathrm{R}}_P \end{bmatrix}, \tag{3}$$

where the submatrix $\bar{\mathbf{Z}}^{\mathrm{R}}_{i,j}$ and the subvector $\mathbf{b}^{\mathrm{R}}_i$ are defined as

$$\begin{cases} \bar{\mathbf{Z}}^{\mathrm{R}}_{i,j} = \bar{\mathbf{J}}^{\mathrm{H}}_i \bar{\mathbf{Z}}_{i,j} \bar{\mathbf{J}}_j & [N_{\mathrm{IPW,SVD},i} \times N_{\mathrm{IPW,SVD},j}] \\ \mathbf{b}^{R}_j = \bar{\mathbf{J}}^{\mathrm{H}}_j \mathbf{b}_j & [N_{\mathrm{IPW,SVD},i} \times 1] \end{cases}. \tag{4}$$

Moreover, the symbol H stands for the conjugate transpose operator and the indexes i and j go from 1 to P. The vector $\mathbf{a}_i$ of Equation (1) is equal to $\mathbf{a}_i = \bar{\mathbf{J}}_i \mathbf{a}^R_i$. The size of the characteristic matrix is $(P\bar{N}_{\mathrm{IPW,SVD}})^2$ instead of $N^2_{\mathrm{Edge}} = (P\bar{N}_{\mathrm{Edge}})^2$ for the whole geometry, where $\bar{N}_{\mathrm{IPW,SVD}} = (1/P)\sum_{p=1}^{P} N_{\mathrm{IPW,SVD},p}$. If multiple excitations $\{\mathbf{b}\}$ (for instance, monostatic case) are considered, then $\bar{\mathbf{Z}}^{\mathrm{R}}$ (or the two matrices of the LU decomposition) and $\{\mathbf{J}_i\}$ must be stored. The reduction factor is $\beta^2 \approx (\bar{N}_{\mathrm{Edge}}/\bar{N}_{\mathrm{IPW,SVD}})^2$ in comparison to the whole matrix.

In Equation (4), to accelerate the matrix-vector product, the coupling matrices $\{\bar{\mathbf{Z}}_{i,j}\}$ are compressed by using the adaptive cross approximation (ACA) [56, 57]. In addition, to further reduce the matrix rank, a second compression based on two QR decompositions, named RACA, is applied. This principle is summarized in [20] and two thresholds $\{\epsilon_{\mathrm{ACA}}, \epsilon_{\mathrm{RACA}}\}$ are then introduced.

The CBFM+ACA parameters are listed in Table 1. For a rough surface and from numerical tests or physical considerations, Bourlier et al. [20] addressed a detailed analysis of the numerical values to

Table 1. Definition of the notations introduced for CBFM and ACA. $\{P, n_{\mathrm{OL}}, \epsilon_{\mathrm{SVD}}, N_{\mathrm{IPW},p}\}$ are the inputs of CBFM. ϵ_{ACA} is the input of ACA. The remained values are numerically obtained from these inputs (outputs).

Name	Definition	Typical values
N_{Edge}	Total number of edges	Table 2
P	Number of blocks	Table 2
n_{OL}	Exceed edges due to the overlapping	1
ϵ_{SVD}	CBFM threshold of the SVD truncation	10^{-3}–10^{-4}
$N_{\mathrm{IPW},p}$	CBFM plane wave number of block p	Eq. (25) of [20]
ϵ_{ACA}	ACA threshold	10^{-3}–10^{-2}
$N_{\mathrm{IPW,SVD},p}$	Reduced value of $N_{\mathrm{IPW},p}$ after a SVD truncation	
$N_{\mathrm{Edge},p}$	Number of edges of a block p	
$N_{\mathrm{Edge,OL},p}$	Number of edges of a block with overlapping	
$\bar{N}_{\mathrm{Edge}} = \sum_{p=1}^{P} N_{\mathrm{Edge},p}$	Mean value of $N_{\mathrm{Edge},p}$ over $p \in [1;P]$	Table 2
$\bar{N}_{\mathrm{IPW}} = \sum_{p=1}^{P} N_{\mathrm{IPW},p}$	Mean value of $N_{\mathrm{IPW},p}$ over $p \in [1;P]$	Figures 2, 4, 5, 7 and 9
$\bar{N}_{\mathrm{IPW,SVD}} = \sum_{p=1}^{P} N_{\mathrm{IPW,SVD},p}$	Mean value of $N_{\mathrm{IPW,SVD},p}$ over $p \in [1;P]$	Table 2
ϵ_{RACA}	RACA threshold	$10\epsilon_{\mathrm{ACA}}$

choose $\{P, n_{\mathrm{OL}}, \epsilon_{\mathrm{SVD}}, N_{\mathrm{IPW},p}, \epsilon_{\mathrm{ACA}}\}$ and their impact on the accuracy of CBFM. From this study, these values has been updated for the scenarii presented in Section 4.

3. CBFM COMBINED WITH THE PHYSICAL OPTICS

3.1. Introduction

From a conventional LU decomposition and for a given block p, Equation (2) implies that the complexity to calculate the $2N_{\mathrm{IPW}}$ PBFs is $2N_{\mathrm{IPW}}\mathcal{O}(N^3_{\mathrm{Edge,OL},p})$. In order to reduce this complexity, the PO approximation can be applied.

Li et al. applied this way for a dielectric rough surface by developing the current-based PO method called the modified equivalent current approximation (MECA) and based on [55], valid for a perfectly-conducting surface. Another way would be to use the MFIE principal value since it is equal to $\mathbf{J} = 2\hat{\mathbf{n}} \times \mathbf{H}_{\mathrm{inc}}$, in which $\hat{\mathbf{n}}$ is the normal to the surface and $\mathbf{H}_{\mathrm{inc}}$ the incident magnetic field, both defined at a given point on the surface. In addition to be consistent with PO, in the shadow region, $\mathbf{J} = \mathbf{0}$.

The discretization of an integral equation (EFIE or MFIE) to obtain the linear system $\bar{\mathbf{Z}}\mathbf{X} = \mathbf{b}$ implies that the impedance matrix $\bar{\mathbf{Z}}$ is independent of the excitation $\mathbf{b}$, related to the incident field, and depends only on the surface geometry. But, since the shadow region is computed from the incident field direction $\hat{\mathbf{k}}_{\mathrm{inc}}$, $\bar{\mathbf{Z}}$ can not contain the information on the shadow region. So, the MFIE principal value of the impedance matrix gives PO if all the points of the surface are viewed by the emitter. For a given excitation, an heuristic approach would be to set to zero the elements of the impedance matrix, for which the edges are in the shadow region given by the criterion $\hat{\mathbf{n}} \cdot \hat{\mathbf{k}}_{\mathrm{inc}} > 0$, where $\hat{\mathbf{n}}$ is the normal to the edge (or mean normal to the two adjacent facets).

For a perfectly-conducting open surface, the EFIE is more accurate than the MFIE, but the EFIE principal value (triangle on itself) is not related to PO, unlike MFIE. To our knowledge, this derivation has never been published in the past; this is the main novelty of this paper and the resulting method is named EFIE PO. The numerical results will show that the based-EFIE PO is more accurate than MECA.

To derive the EFIE PO impedance matrix, we start from EFIE and we calculate the resulting Green function that obeys the PO approximation. Theoretically, it is important to underline that the Green function G characterizes the propagation from a source point of coordinates $\mathbf{r}$ to the observation point $\mathbf{r}'$. This means that G should be independent of the excitation.

3.2. EFIE PO Green Function

From the EFIE [1] (Equation (2.119)), one can write

$$-\frac{j}{\omega\mu_0}\,\mathbf{E}_{\mathrm{inc}}(\mathbf{r}') = \iint_S \boldsymbol{\mathcal{K}}\left(\mathbf{r}', \mathbf{r}\right) d\mathbf{r}, \tag{5}$$

where the kernel $\boldsymbol{\mathcal{K}}(\mathbf{r}', \mathbf{r}) = G(\mathbf{r}', \mathbf{r})[\mathbf{J}(\mathbf{r}) + \boldsymbol{\nabla}(\boldsymbol{\nabla} \cdot \mathbf{J}(\mathbf{r}))/k^2]$. G stands for the Green function, k the wave number, $\mathbf{r}'$ an observation point, $\mathbf{r}$ a point on the surface, $\mathbf{E}_{\mathrm{inc}}$ the incident electric field, ω the pulsation frequency and μ_0 the permeability of the vacuum.

In the lit region, the PO approximation assumes that the surface current equals $\mathbf{J}(\mathbf{r}) = 2\hat{\mathbf{n}}(\mathbf{r}) \times \mathbf{H}_{\mathrm{inc}}(\mathbf{r})$, where $\mathbf{H}_{\mathrm{inc}}$ stands for the incident magnetic field. Then

$$\begin{aligned} \boldsymbol{\nabla} \cdot \mathbf{J}(\mathbf{r}) &= 2\boldsymbol{\nabla} \cdot [\hat{\mathbf{n}}(\mathbf{r}) \times \mathbf{H}_{\mathrm{inc}}(\mathbf{r})] = 2\left[(\boldsymbol{\nabla} \times \hat{\mathbf{n}}) \cdot \mathbf{H}_{\mathrm{inc}} - \hat{\mathbf{n}} \cdot (\boldsymbol{\nabla} \times \mathbf{H}_{\mathrm{inc}})\right] \\ &\approx -2\hat{\mathbf{n}} \cdot (\boldsymbol{\nabla} \times \mathbf{H}_{\mathrm{inc}}), \end{aligned} \tag{6}$$

since $\boldsymbol{\nabla} \times \hat{\mathbf{n}} \approx \mathbf{0}$ related to the surface curvature, which is consistent with the PO approximation. Moreover

$$\begin{aligned} \boldsymbol{\nabla}\left[\boldsymbol{\nabla} \cdot \mathbf{J}(\mathbf{r})\right] &= -2\boldsymbol{\nabla}\left[\hat{\mathbf{n}} \cdot (\boldsymbol{\nabla} \times \mathbf{H}_{\mathrm{inc}})\right] \\ &\approx -2\Big\{ \left(\hat{\mathbf{n}} \cdot \boldsymbol{\nabla}\right)(\boldsymbol{\nabla} \times \mathbf{H}_{\mathrm{inc}}) + \hat{\mathbf{n}} \times \Big[\boldsymbol{\nabla} \times (\boldsymbol{\nabla} \times \mathbf{H}_{\mathrm{inc}})\Big\}\Big], \end{aligned} \tag{7}$$

because for any vectorial function $\mathbf{A}(\mathbf{r})$ and $\mathbf{B}(\mathbf{r})$, $\boldsymbol{\nabla}(\mathbf{A}\cdot\mathbf{B}) = (\mathbf{A}\cdot\boldsymbol{\nabla})\mathbf{B} + (\mathbf{B}\cdot\boldsymbol{\nabla})\mathbf{A} + \mathbf{A}\times(\boldsymbol{\nabla}\times\mathbf{B}) + \mathbf{B}\times(\boldsymbol{\nabla}\times\mathbf{A})$, where $\mathbf{A} = \hat{\mathbf{n}}$ and $\mathbf{B} = \boldsymbol{\nabla}\times\mathbf{H}_{\text{inc}}$, for which $(\mathbf{B}\cdot\boldsymbol{\nabla})\hat{\mathbf{n}} \approx \mathbf{0}$ and $\boldsymbol{\nabla}\times\hat{\mathbf{n}} \approx \mathbf{0}$.

For any vectorial function $\mathbf{A}(\mathbf{r})$, the **curl** vectorial operator $\mathbf{curlA} = \boldsymbol{\nabla}\times\mathbf{A}$. From a Maxwell's equation, we can show that

$$\boldsymbol{\nabla}\times(\boldsymbol{\nabla}\times\mathbf{H}_{\text{inc}}) = -\boldsymbol{\nabla}^2\mathbf{H}_{\text{inc}} + \boldsymbol{\nabla}(\boldsymbol{\nabla}\cdot\mathbf{H}_{\text{inc}}) = -\boldsymbol{\nabla}^2\mathbf{H}_{\text{inc}}, \tag{8}$$

since $\boldsymbol{\nabla}\cdot\mathbf{H}_{\text{inc}} = \text{div}\mathbf{H}_{\text{inc}} = 0$. Then

$$\boldsymbol{\nabla}[\boldsymbol{\nabla}\cdot\mathbf{J}(\mathbf{r})] \approx -2\Big\{(\hat{\mathbf{n}}\cdot\boldsymbol{\nabla})(\boldsymbol{\nabla}\times\mathbf{H}_{\text{inc}}) - \hat{\mathbf{n}}\times\left(\boldsymbol{\nabla}^2\mathbf{H}_{\text{inc}}\right)\Big\}. \tag{9}$$

With the time convention $e^{-j\omega t}$ and a Maxwell's equation, $\boldsymbol{\nabla}\times\mathbf{H}_{\text{inc}} = \epsilon_0\partial_t\mathbf{E}_{\text{inc}} = -j\omega\epsilon_0\mathbf{E}_{\text{inc}}$ where ϵ_0 is the vacuum permittivity and $\partial_t = \partial/\partial t$. The use of the wave propagation leads to $\boldsymbol{\nabla}^2\mathbf{H}_{\text{inc}} = \mu_0\epsilon_0\partial_t^2\mathbf{H}_{\text{inc}} = -\mu_0\epsilon_0\omega^2\mathbf{H}_{\text{inc}}$.

The above equation is simplified as

$$\begin{aligned}\boldsymbol{\nabla}[\boldsymbol{\nabla}\cdot\mathbf{J}(\mathbf{r})] &\approx 2\Big[j\omega\epsilon_0(\hat{\mathbf{n}}\cdot\boldsymbol{\nabla})\mathbf{E}_{\text{inc}} - \mu_0\epsilon_0\omega^2\hat{\mathbf{n}}\times\mathbf{H}_{\text{inc}}\Big]\\ &\approx 2j\omega\epsilon_0(\hat{\mathbf{n}}\cdot\boldsymbol{\nabla})\mathbf{E}_{\text{inc}} - 2k^2\hat{\mathbf{n}}\times\mathbf{H}_{\text{inc}},\end{aligned} \tag{10}$$

where $\mu_0\epsilon_0\omega^2 = k^2$. Finally, the use of PO leads to

$$\mathbf{J}(\mathbf{r}) + \frac{\boldsymbol{\nabla}[\boldsymbol{\nabla}\cdot\mathbf{J}(\mathbf{r})]}{k^2} \approx \frac{2j\omega\epsilon_0}{k^2}(\hat{\mathbf{n}}\cdot\boldsymbol{\nabla})\mathbf{E}_{\text{inc}}. \tag{11}$$

The boundary condition implies that the tangent component of the electric field $\hat{\mathbf{t}}\cdot\mathbf{E}_{\text{inc}} = E_t$ is continuous, where $\hat{\mathbf{t}}$ is a vector tangent to the surface. The substitution of Equation (11) into Equation (5) yields

$$E_t(\mathbf{r}') = -2\iint_S G(\mathbf{r}',\mathbf{r})(\hat{\mathbf{n}}(\mathbf{r})\cdot\boldsymbol{\nabla})E_t(\mathbf{r})d\mathbf{r}. \tag{12}$$

We can note

$$(\hat{\mathbf{n}}\cdot\boldsymbol{\nabla})E_t = \hat{\mathbf{n}}\cdot\boldsymbol{\nabla}E_t = (\hat{\mathbf{n}}\cdot\hat{\mathbf{r}})\frac{\partial E_t}{\partial r}, \tag{13}$$

since for any vector $\mathbf{r} = (x,y,z)$ and scalar function $f(\mathbf{r})$, we have

$$\begin{aligned}\boldsymbol{\nabla}f &= \hat{\mathbf{x}}\frac{\partial f}{\partial x} + \hat{\mathbf{y}}\frac{\partial f}{\partial y} + \hat{\mathbf{z}}\frac{\partial f}{\partial z} = \hat{\mathbf{x}}\frac{\partial f}{\partial r}\frac{\partial r}{\partial x} + \hat{\mathbf{y}}\frac{\partial f}{\partial r}\frac{\partial r}{\partial y} + \hat{\mathbf{z}}\frac{\partial f}{\partial r}\frac{\partial r}{\partial z} = \hat{\mathbf{x}}\frac{\partial f}{\partial r}\frac{x}{r} + \hat{\mathbf{y}}\frac{\partial f}{\partial r}\frac{y}{r} + \hat{\mathbf{z}}\frac{\partial f}{\partial r}\frac{z}{r}\\ &= \frac{\mathbf{r}}{r}\frac{\partial f}{\partial r} = \hat{\mathbf{r}}\frac{\partial f}{\partial r},\end{aligned} \tag{14}$$

where $r = \sqrt{x^2+y^2+z^2}$ and $\mathbf{r} = \hat{\mathbf{x}}x + \hat{\mathbf{y}}y + \hat{\mathbf{z}}z$.

In addition, since the gradient $\boldsymbol{\nabla}E_t$ is a vector normal to the surface, the scalar product with the normal $\hat{\mathbf{n}}$ is one. For a surface with a small curvature, to be consistent with PO, this implies that $\hat{\mathbf{n}}\cdot\hat{\mathbf{r}} \approx 1$. Therefore, taking the partial derivative over r' of Equation (12), we obtain

$$F_t(\mathbf{r}') = -2\iint_S \frac{\partial G(\mathbf{r}',\mathbf{r})}{\partial r'}F_t(\mathbf{r})d\mathbf{r}, \tag{15}$$

where $F_t = \partial E_t/\partial r$. Moreover

$$\frac{\partial G(\mathbf{r}',\mathbf{r})}{\partial r'} = -jkG(\mathbf{r}',\mathbf{r})\left(1 + \frac{1}{jkr'}\right) \approx -jkG(\mathbf{r}',\mathbf{r}). \tag{16}$$

The above equation assumes that $|kr| \gg 1$ (far field approximation). Since the Green function depends on the difference $\|\mathbf{r}'-\mathbf{r}\|$ and from Equation (16), Equation (15) takes the form $F_t = 2jk(G * F_t)$, where $*$ is the convolution product. Thus, under the PO approximation, the Green function writes

$$G(\mathbf{r}',\mathbf{r}) = \frac{1}{2jk}\delta(\mathbf{r}'-\mathbf{r}), \tag{17}$$

where δ is the two-dimensional delta function. As expected, this means that the resulting PO Green function depends only on a single point. In other words, it is local, that is, no multiple reflection. The multiple refections will be accounted for by decomposing the geometry into sub-geometries and by introducing the coupling matrices.

3.3. EFIE PO Impedance Matrix

In Equation (17), the Dirac delta function $\delta(\mathbf{r}'-\mathbf{r})$ contributes if $\mathbf{r}'=\mathbf{r}$. This implies that

$$\iint_S G\left(\mathbf{r}',\mathbf{r}\right)\boldsymbol{\nabla}\left(\boldsymbol{\nabla}\cdot\mathbf{J}(\mathbf{r})\right)d\mathbf{r}=\boldsymbol{\nabla}'\left(\boldsymbol{\nabla}'\cdot\mathbf{J}(\mathbf{r}')\right), \tag{18}$$

where the operator $\boldsymbol{\nabla}'$ acts on the vector $\mathbf{r}'$. From the RWG basis function $\mathbf{f}_n(\mathbf{r}')=\mathbf{f}'_n$, $\boldsymbol{\nabla}'\cdot\mathbf{f}'_n$ is a constant, which implies that $\boldsymbol{\nabla}'\boldsymbol{\nabla}'\cdot\mathbf{f}'_n=\mathbf{0}$.

Substituting Equation (17) into Equation (5), applying the boundary conditions (continuity of the tangent component) and the Galerkin method of moments with RWG basis function $\mathbf{f}_n$ [1] (Equation (7.11)), an element of the resulting impedance matrix equals

$$\begin{aligned} Z_{m,n} &= \frac{1}{2jk}\iint_{S_m}\iint_{S_n}\mathbf{f}_m(\mathbf{r})\cdot\mathbf{f}_n(\mathbf{r}')\delta\left(\mathbf{r}'-\mathbf{r}\right)d\mathbf{r}d\mathbf{r}'=\frac{1}{2jk}\iint_{\mathbf{f}_n=\mathbf{f}_m}\mathbf{f}_m(\mathbf{r})\cdot\mathbf{f}_n(\mathbf{r})d\mathbf{r} \\ &= \frac{\mathrm{PV}\left(\mathrm{MFIE}\right)}{jk}, \end{aligned} \tag{19}$$

where PV stands for the principal value. Equation (19) clearly shows that the EFIE PO is obtained from the PV of MFIE divided by the factor jk. Physically, the PV (represented mathematically by the Dirac delta function in Equation (17)) means that the impedance matrix accounts only for the local interactions (triangle on itself), which is consistent with PO, since the multiple reflections are neglected.

Doing analytically the integration over $\mathbf{r}$ of Equation (19), $Z_{m,n}$ can be expressed as

$$Z_{m,n}=\frac{c_{m,n}}{12jk}\left\{\sum_{i=1}^{3}\left(\|\mathbf{V}_i\|^2+\mathbf{V}_1\cdot\mathbf{V}_2+\mathbf{V}_1\cdot\mathbf{V}_3+\mathbf{V}_2\cdot\mathbf{V}_3\right)+6\left[\mathbf{V}_m\cdot\mathbf{V}_n-\mathbf{V}_G\cdot(\mathbf{V}_m+\mathbf{V}_n)\right]\right\}, \tag{20}$$

where $\{\mathbf{V}_i\}$ are the coordinates of the three vertices of the triangular facet, $\mathbf{V}_G$ its gravity center and $\{\mathbf{V}_{m,n}\}$ the unshared vertices. Moreover, $c_{m,n}=s_m s_n L_m L_n/(4A)$, where $s_m=\pm1$, $s_n=\pm1$, $L_{m,n}$ the edge length and A the facet area.

Equation (19) shows that the PO impedance matrix is sparse since a facet interacts only with itself (no multiple reflections). This involves that only $4N_{\mathrm{Edge},p}$ elements of the sub-impedance matrix are calculated (instead of $N^2_{\mathrm{Edge},p}$). Lucente et al. [59] proposed a similar way to accelerate the computation of the PBFs by calculating only the elements of the EFIE sub-impedance matrix, for which the interaction length between the edges does not exceed 0.15λ. By comparing this approach with the previous one, numerical results show that PO approximation is more accurate.

Since the PO impedance matrix is sparse, to solve the resulting linear system, the use of iterative algorithms can be very efficient if the number of iterations is small. Sub-section 4.6 will address one which has these features.

4. NUMERICAL RESULTS

The computer machine is Intel(R) Xeon(R) Gold 6142 CPU @ 2.60 GHz (4 processors) with 768 GB (needed for the brute force of MoM, that is EFIE-LU) of RAM. The wavelength in free space λ is 1 m. The azimuthal incident and scattering angles are $\phi_{\mathrm{inc}}=\phi_{\mathrm{sca}}=0$. Table 2 lists the parameters of the simulations. In comparison to the whole matrix of size $N_{\mathrm{Edge}}\times N_{\mathrm{Edge}}$ ($N_{\mathrm{Edge}}=P\bar{N}_{\mathrm{Edge}}$), the size of the CBFM characteristic matrix is $N_R\times N_R$, where $N_R=P\bar{N}_{\mathrm{IPW,SVD}}$. In the legend of the figures, $[\bar{N}_{\mathrm{IPW}}\Rightarrow\bar{N}_{\mathrm{IPW,SVD}}]$ is given.

4.1. Smooth Plate of Area $(6\lambda)^2$

First a smooth plate (without thickness) is considered. It lies on the (Ox,Oy) plane and centered at $(0,0,0)$ and its surface area is L_xL_y, where $\{L_{x,y}\}$ are the surface lengths with respect to the $\hat{\mathbf{x}}$ and $\hat{\mathbf{y}}$ directions. The sampling steps with respect to the $\hat{\mathbf{x}}$ and $\hat{\mathbf{y}}$ directions are equal $\Delta x=\Delta y=0.1\lambda$.

Figures 1 and 2 plot the RCS in dBm^2 versus the scattering angle θ_{sca} for lengths $L_x=L_y=6\lambda$ (number of edges $N_{\mathrm{Edge}}=10,680$). The incident angle is $\theta_{\mathrm{inc}}=0$. The specular direction is defined as $-\theta_{\mathrm{inc}}=0$ and the polarization is VV. The simulation parameters are listed in Table 2.

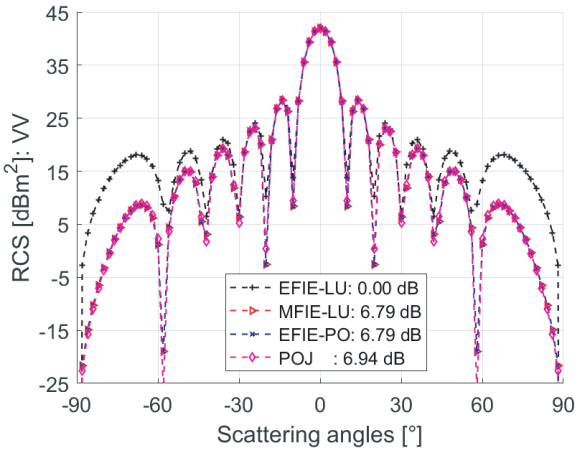

Figure 1. RCS in dBm^2 versus the scattering angle θ_{sca}. Square plate of lengths $L_x = L_y = 6\lambda$, $\theta_{\text{inc}} = 0$ and the polarization is VV. The simulation parameters are listed in Table 2.

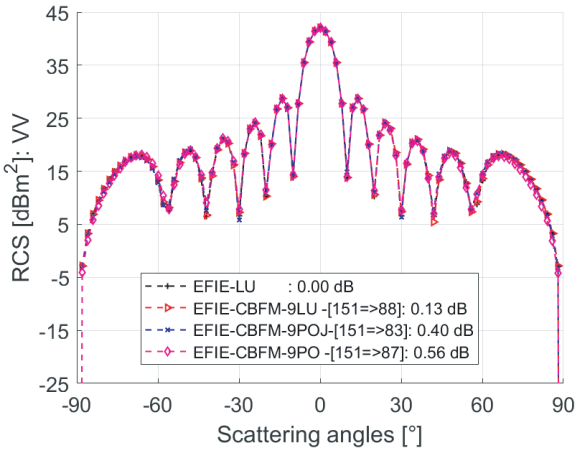

Figure 2. Same as in Fig. 1 but the results of EFIE-CBFM are shown. The simulation parameters are listed in Table 2.

Table 2. Parameters of the simulations. $n_{\text{OL}} = 1$ for all scenarii.

Geometry	P	N_{Edge}	$\bar{N}_{\text{Edge}}$	$\bar{N}_{\text{Edge,OL}}$	$\bar{N}_{\text{IPW,SVD}}$	ϵ_{CBFM}
Plate	9	10,680	1187	1323	88	10^{-3}
Sphere	8	10,806	1351	1519	41	10^{-3}
Dihedral	8	9,480	1185	1344	106	10^{-3}
Open cavity	24	62,320	2597	2915	211	10^{-4}
Paraboloid	36	24,120	670	856	99	10^{-3}

In the legend, the labels mean:

- EFIE-LU: EFIE and the linear system is solved from a LU decomposition (reference solution).
- MFIE-LU: MFIE and the linear system is solved from a LU decomposition.
- EFIE-PO: EFIE is computed from the PO impedance matrix derived in Section 3.3.
- POJ : The $\{a_n\}$ coefficients (unknowns of the linear system $\bar{\mathbf{Z}}\mathbf{a} = \mathbf{b}$) are computed from PO derived in Reference [55] (the linear system is not solved).
- EFIE-CBFM-PMethod-[$\bar{N}_{\text{IPW}} \Rightarrow \bar{N}_{\text{IPW,SVD}}$] ($P = 9$ and a block of area $(2\lambda)^2$), where 'Method" is the method applied to calculate the PBFs of a block. It can be "LU" (calculated from a LU decomposition of the sub-impedance matrix), "POJ" (calculated from the PO published in [55]) and "PO" (computed from the PO impedance matrix derived in Section 3.2).

In addition, the last number "Dif" in the legend, is the mean difference in dB scale (ratio in linear scale) over the $N_{\theta_{\text{sca}}}$ scattering angles against the reference method "EFIE-LU". It is defined as

$$\text{Dif} = \frac{1}{N_{\theta_{\text{sca}}}} \sum_{\theta_{\text{sca}}} 10 \left| \log_{10} \left(\frac{\text{RCS}}{\text{RCS}_{\text{EFIE-LU}}} \right) \right|. \tag{21}$$

As expected, around the specular direction (near 0 degree), Fig. 1 shows that the PO results of the different formulations match well with those obtained from EFIE-LU. Far from this direction, they strongly deviate because PO neglects the edge diffraction. For a smooth plate, the principle value of MFIE only contributes (because no curvature) which equals PO when no shadow occurs. If a thin smooth plate (typically of thickness of 0.1λ) is considered, then a very good agreement between EFIE-LU and MFIE-LU is obtained. But the number of unknowns is approximated twice larger, which needs more numerical resources.

In other hand, Fig. 2 shows that the EFIE-CBFM-9LU results coincide with those of EFIE-LU. Moreover, those computed from CBFM combined with PO match very well with EFIE-LU. It is important to underline that this means that the edge diffraction is accounted for in CBFM although the PBFs are calculated from PO. As pointed out by Lucente et al. [59], even if the PFBs are approximated, thanks to the second step of CBFM consisting in calculating the characteristic impedance matrix, CBFM gives good results.

From Table 2 the reduction factor $N_{\text{Edge}}/N_R = 10,680/(9 \times 88) \approx 13.5$.

4.2. Sphere of Radius Equals 0.8λ

To test the performances of CBFM combined with PO, a geometry with a curvature depicted in Fig. 3 is considered: A sphere of radius equals 0.8λ and the edge mean length is 0.05λ. The simulation parameters are listed in Table 2.

Figure 4 plots the RCS in dBm^2 versus the scattering angle θ_{sca}. The incident angle is $\theta_{\text{inc}} = 0$ and the polarization is VV. In addition, the reference Mie solution ([60], Section 6.1) is plotted. As expected, the EFIE-LU results match well those of Mie, as well those computed from CBFM-8LU and

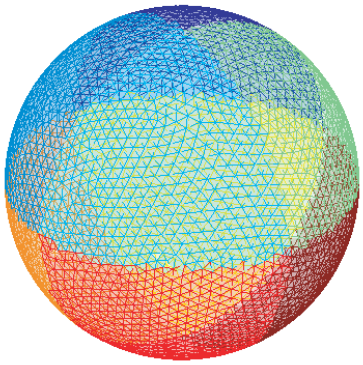

Figure 3. Sphere of radius equals 0.8λ ($N_{\text{Edge}} = 10,806$). A block is represented by a color and the edge mean length is 0.05λ. The simulation parameters are listed in Table 2.

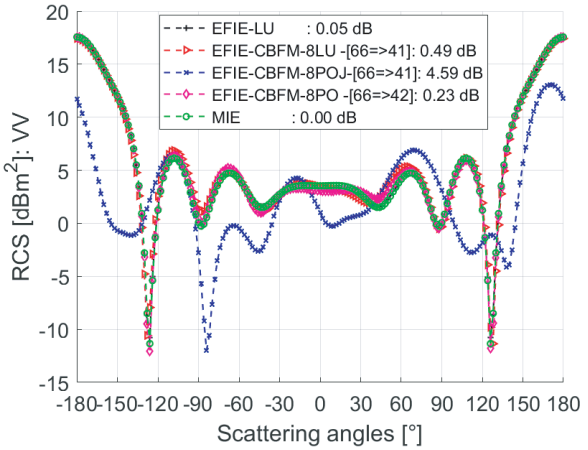

Figure 4. RCS in dBm^2 versus the scattering angle θ_{sca}. Sphere of radius equals 0.8λ ($N_{\text{Edge}} = 10,806$ and the geometry is shown in Fig. 3), $\theta_{\text{inc}} = 0$ and the polarization is VV. The simulation parameters are listed in Table 2.

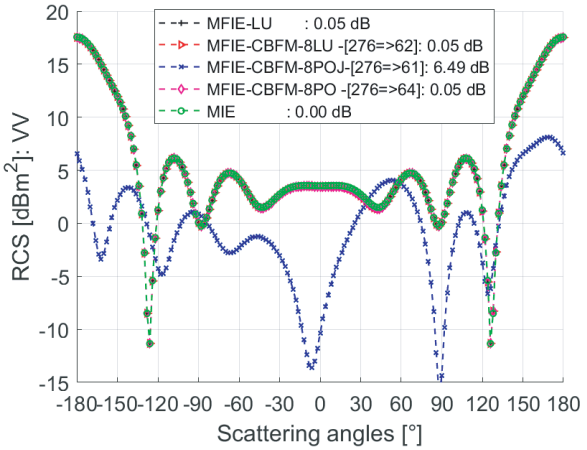

Figure 5. Same variations as in Fig. 4 but the MFIE is applied.

CBFM-8PO, except those obtained from CBFM-8POJ (PO published in [55]). This means that POJ is inaccurate for the calculation of the PBFs for an object with a curvature. The results computed from "CBFM-8PO" are slightly better than those obtained by "CBFM-8LU" because the number of PBFs $\bar{N}_{\mathrm{IPW,SVD}}$ is slightly larger (42 and 41, respectively).

From Table 2, the reduction factor $N_{\mathrm{Edge}}/N_R = 10,806/(8 \times 41) \approx 33$.

Figure 5 plots the same variations as in Fig. 4 but the MFIE is applied. As we can see, a good agreement is obtained between the different models except when "POJ" (PO published in [55]) is applied for the calculation of the PBFs. In comparison to EFIE-CBFM, more PBFs are needed (62 instead of 41 for EFIE), which explains that the MFIE-CBFM results are slightly better.

4.3. Dihedral with Defaults

To exhibit at least two reflections, a dihedral is considered in Fig. 6. It is composed of two identical plates of area $(4\lambda)^2$ with 4 defaults of Gaussian shapes with an amplitude $a = 0.5\lambda$. In addition, the plates are orthogonal.

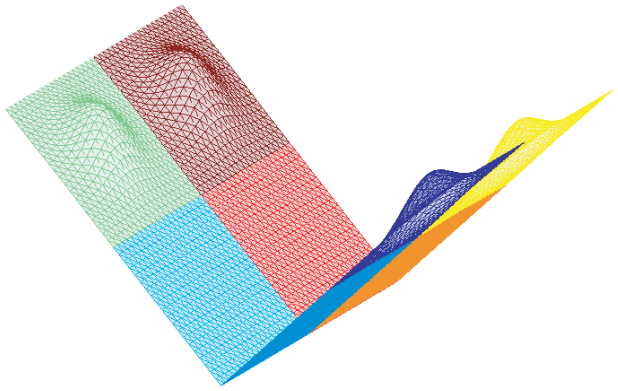

Figure 6. Dihedral composed of two identical plates of area $(4\lambda)^2$ with 4 defaults of Gaussian shapes with an amplitude $a = 0.5\lambda$. In addition, the plates are orthogonal. The total number of blocks $P = 8$ (area $(2\lambda)^2$ and plotted in different colors) and the 4 defaults are included into 4 blocks. The simulation parameters are listed in Table 2.

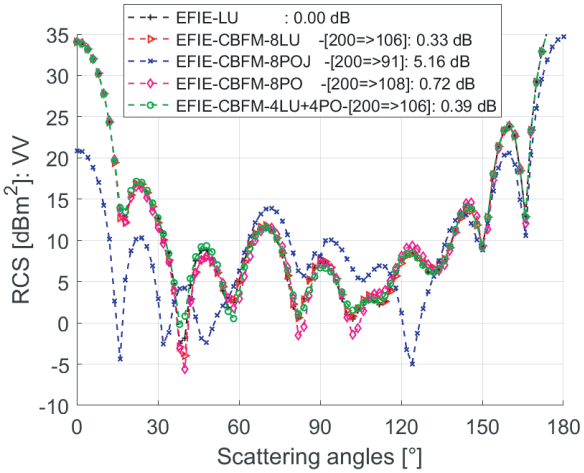

Figure 7. RCS in dBm^2 versus the scattering angle θ_{sca}. The geometry is shown in Fig. 6 and the polarization is VV. The simulation parameters are listed in Table 2.

Figure 7 plots the corresponding RCS in dBm^2 versus the scattering angle θ_{sca}. The simulation parameters are listed in Table 2. As we can see, CBFM-8LU perfectly matches with the reference method EFIE-LU and CBFM combined with the PO impedance matrix (CBFM-8PO and CBFM-4LU+4PO) predicts satisfactory results. Nevertheless, the comparison of CBFM-8POJ with EFIE+LU is not satisfactory. For the PBFs computation, the domain decomposition method is able to apply either LU or PO on each block. For CBFM-4LU+4PO, LU is applied on the 4 blocks with defaults and for the 4 remaining blocks, PO is used. As expected, the comparison of CBFM-4LU+4PO with CBFM-8LU shows that the use of LU on the blocks with defaults slightly improves the results. The local default has an amplitude of $a = 0.5\lambda$ and the area block is $(2\lambda)^2$. This implies that the mean slope of the default is of the order of $a/\lambda = 0.5$ and the PO approximation may be failed.

From Table 2, the reduction factor $N_{\mathrm{Edge}}/N_R = 9,480/(8 \times 106) \approx 11.2$.

4.4. Open-ended Cavity of Size $4 \times 4 \times 12\lambda^3$ with 1 Default

To exhibit multiple reflections, an open-ended cavity is considered in Fig. 8. The total number of blocks is $P = 24$ and the single default of a Gaussian shape with an amplitude $|a| = 1\lambda$) (located at the bottom) is included into 4 blocks.

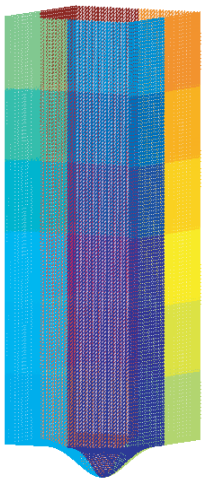

Figure 8. Open-ended cavity of size $4 \times 4 \times 12\lambda^3$ with 1 default of Gaussian shape ($a = -0.5\lambda$). The total number of blocks is $P = 24$ and the single default (located at the bottom) is included into 4 blocks. The simulation parameters are listed in Table 2.

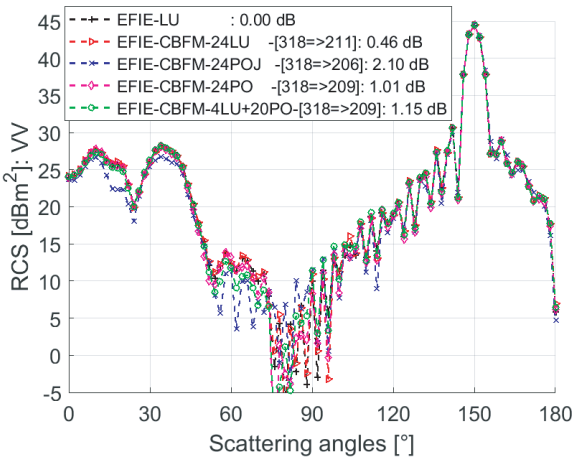

Figure 9. RCS in dBm^2 versus the scattering angle θ_{sca}. The geometry is shown in Fig. 8, the polarization is VV and $\theta_{\mathrm{inc}} = -\pi/6$. The simulation parameters are listed in Table 2.

Figure 9 plots the corresponding RCS in dBm^2 versus the scattering angle θ_{sca}. The polarization is VV and $\theta_{\mathrm{inc}} = -\pi/6$. The simulation parameters are listed in Table 2. In addition, in comparison to the three previous geometries, the number of PBFs $\bar{N}_{\mathrm{IPW}}$ is multiplied by 2 and the threshold $\epsilon_{\mathrm{CBFM}} = 10^{-4}$ (instead of 10^{-3}) to obtain more-accurate results. As we can see in Fig. 9, CBFM-24LU still predicts very good results and CBFM combined with PO, except POJ, give satisfactory results.

From Table 2 the reduction factor $N_{\mathrm{Edge}}/N_R = 62,320/(24 \times 211) \approx 12.3$.

4.5. Paraboloid of Size $9 \times 9\lambda^2$

To exhibit multiple reflections for an object with curvature, a paraboloid is considered in Fig. 10. The total number of blocks is $P = 36$. Fig. 11 plots the corresponding RCS in dBm^2 versus the scattering angle θ_{sca}. The polarization is VV and $\theta_{\mathrm{inc}} = -\pi/6$. The simulation parameters are listed in Table 2. As we can see in Fig. 11, CBFM-36LU predicts very good results and, CBFM-36PO combined with PO and RACA (for the compression of the coupling matrices) give satisfactory results. Some differences occur for low strengths of the RCS. In the legend of Fig. 11, the numbers with an exponent indicate the RACA thresholds ($\epsilon_{\mathrm{ACA}}, \epsilon_{\mathrm{RACA}} = 10\epsilon_{\mathrm{ACA}}$). The last number equals the mean RACA compression ratio $\bar{\tau}_{\mathrm{RACA}}$. If $\tau_{\mathrm{RACA}} = 1$, then a coupling matrix can only be nearly expressed as the product of a single column vector by a single row vector.

It is well known that ACA algorithm is efficient for two "far" blocks. Thus, for blocks sharing at least one vertex, ACA is not applied. This means in Fig. 10 that ACA is applied on 1090 block pairs over a total of $36^2 = 1296$. As we can see in Fig. 11, as ($\epsilon_{\mathrm{ACA}}, \epsilon_{\mathrm{RACA}} = 10\epsilon_{\mathrm{ACA}}$) increases, the ACA compression ratio increases and it is closer of 1, implying that RACA is very efficient. In addition, the precision on the RCS remains satisfactory.

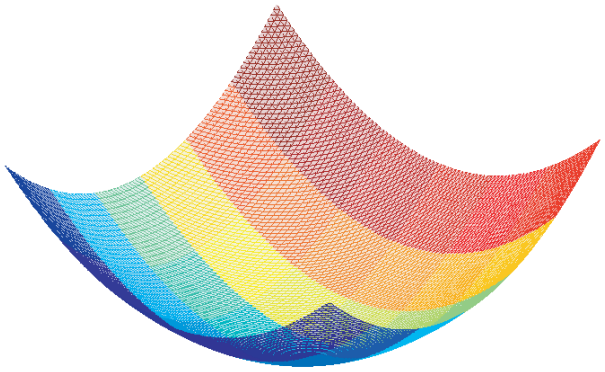

Figure 10. Paraboloid of size $9 \times 9\lambda^2$ with an amplitude of $a = 4.5\lambda$. The total number of blocks is $P = 36$. The simulation parameters are listed in Table 2.

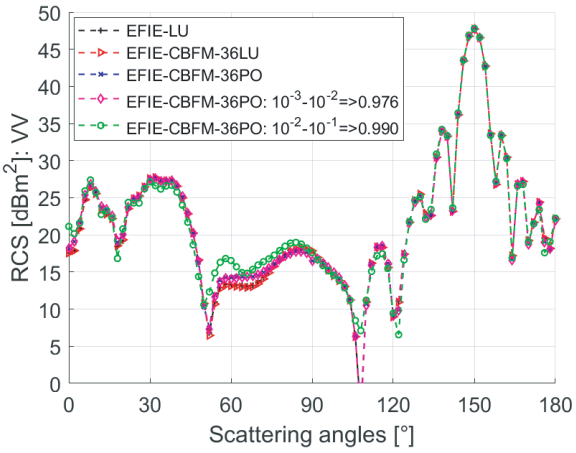

Figure 11. RCS in dBm^2 versus the scattering angle θ_{sca}. The geometry is shown in Fig. 10, the polarization is VV and $\theta_{\mathrm{inc}} = -\pi/6$. The simulation parameters are listed in Table 2.

4.6. PBFs Computation Acceleration from Iterative Algorithms

It is important to underline that the PO impedance matrix $\bar{\mathbf{Z}}_{\mathrm{PO}}$ is nearly diagonal. A simple means to solve the linear system $\bar{\mathbf{Z}}_{\mathrm{PO}}\mathbf{X} = \mathbf{b}$ is to write

$$\begin{aligned}\mathbf{X} &= \bar{\mathbf{Z}}_{\mathrm{PO}}^{-1}\mathbf{b} = \left(\bar{\mathbf{Z}}_{\mathrm{D}} + \bar{\mathbf{\Delta}}_Z\right)^{-1}\mathbf{b} = \left[\bar{\mathbf{Z}}_{\mathrm{D}}\left(\bar{\mathbf{I}} + \bar{\mathbf{Z}}_{\mathrm{D}}^{-1}\bar{\mathbf{\Delta}}_Z\right)\right]^{-1}\mathbf{b} \\ &= \left(\bar{\mathbf{I}} + \bar{\mathbf{M}}_c\right)^{-1}\bar{\mathbf{Z}}_{\mathrm{D}}^{-1}\mathbf{b} \\ &\approx \sum_{k=0}^{K}\left(-\bar{\mathbf{M}}_c\right)^k\bar{\mathbf{Z}}_{\mathrm{D}}\mathbf{b} = \sum_{k=0}^{K}\bar{\mathbf{Y}}^{(k)},\end{aligned} \tag{22}$$

in which

$$\begin{cases}\bar{\mathbf{Y}}^{(0)} = \bar{\mathbf{Z}}_{\mathrm{D}}\mathbf{b} & k = 0 \\ \bar{\mathbf{Y}}^{(k+1)} = -\bar{\mathbf{M}}_c\bar{\mathbf{Y}}^{(k)} & k > 0\end{cases}. \tag{23}$$

This algorithm converges if the spectral radius (largest modulus of its eigenvalues) of $\bar{\mathbf{M}}_c = \bar{\mathbf{Z}}_D^{-1}\bar{\mathbf{\Delta}}_Z$ is strictly smaller than one. The matrix $\bar{\mathbf{Z}}_{\mathrm{D}}$ is the diagonal part of $\bar{\mathbf{Z}}_{\mathrm{PO}}$ and the sparse matrix is defined as $\bar{\mathbf{\Delta}}_Z = \bar{\mathbf{Z}}_{\mathrm{PO}} - \bar{\mathbf{Z}}_{\mathrm{D}}$ and has only $3N_{\mathrm{Edge}}$ non zero values. Thus, the calculation of $\bar{\mathbf{M}}_c\bar{\mathbf{Y}}^{(k)}$ requires only $3N_{\mathrm{Edge}} + N_{\mathrm{Edge}} = 4N_{\mathrm{Edge}}$ multiplications instead of N_{Edge}^2 for a full matrix. The complexity of the above iterative method is $\mathcal{O}(4KN_{\mathrm{Edge}})$, where K is the convergence order obtained by setting a threshold.

Figure 12 plots the RCS in dBm^2 versus the scattering angle θ_{sca}. The simulation parameters are the same as in Fig. 11. In addition, in the legend "LU" means "EFIE+LU" and the last 3 curves are obtained from EFIE-CBFM combined with PO. The label "IT$\bar{K}$" means that the PFBs are computed from Equation (22) and the mean convergence order $\bar{K} = 12$, whereas for "GC$\bar{K}$" (function bicg in MatLab), they are computed from the gradient conjugate method and $\bar{K} = 8$. For the both methods, the threshold equals 10^{-3}. As we can see, the two iterative methods predict good results in comparison to 36PO and converge rapidly.

4.7. Complexity and Comments on the MatLab Software

Figure 13 plots the filling time in seconds to calculate the whole impedance matrix (for LU) and the sub-matrices of CBFM. Figs. 14 and 15 plot the numerical and theoretical complexities in seconds (the time filling is not included), respectively. The geometry shape is shown in Fig. 10 of size $L \times L$, where

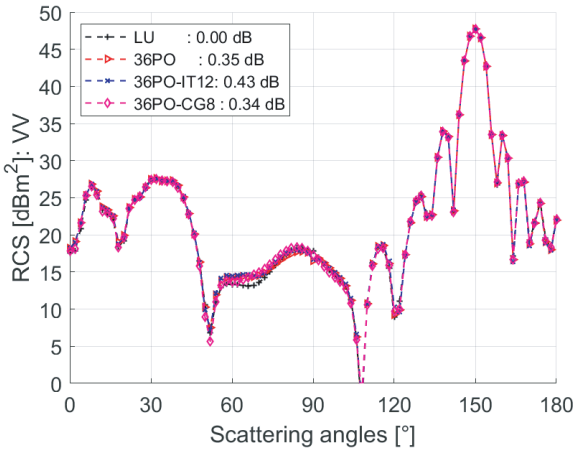

Figure 12. RCS in dBm^2 versus the scattering angle θ_{sca}. The simulation parameters are the same as in Fig. 11. In addition, in the legend "LU" means "EFIE+LU" and the last 3 curves are obtained from EFIE-CBFM combined with PO.

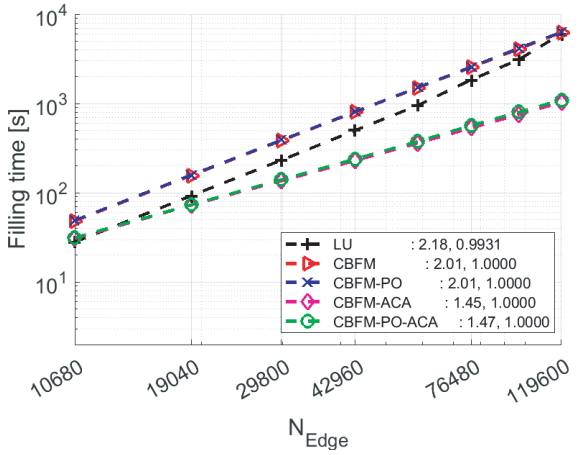

Figure 13. Filling time in seconds to calculate the whole impedance matrix (for LU) and the sub-matrices of CBFM. The EFIE is applied.

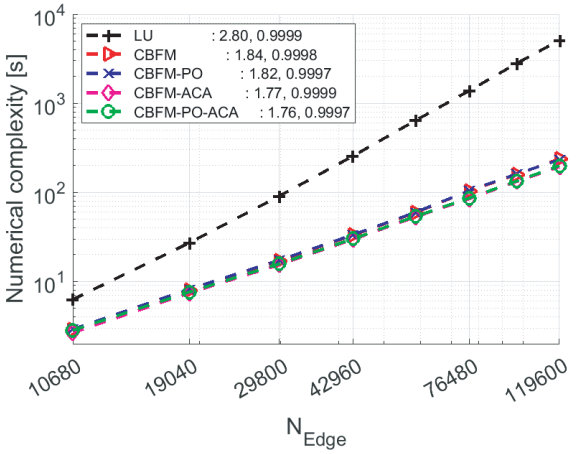

Figure 14. Numerical complexity in seconds (the filling time is not included). The EFIE is applied.

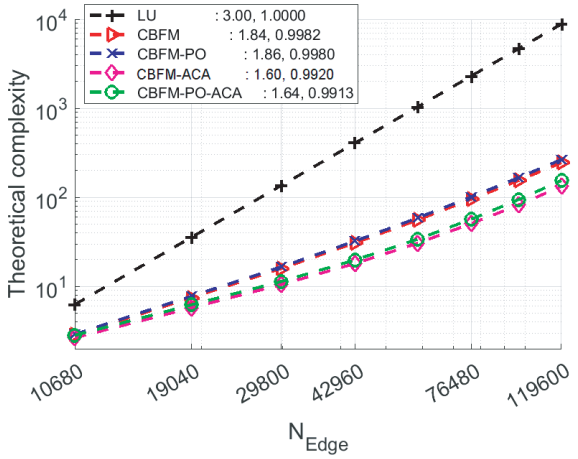

Figure 15. Theoretical complexity in seconds (the filling time is not included). The EFIE is applied.

the length L ranges from 6λ to 16λ and the amplitude $a = L/2$ (the slopes are constant with respect to L). The number of edges N_{Edge} ranges from 10,680 to 119,600 and the size of the blocks $(2\lambda)^2$ are constant (their number ranges from 9 to 100). The EFIE is applied. The complexity is modeled as $C = aN_{\text{Edge}}^n$, in which (a, n) are obtained from a linear regression. The value of n (with 2 digits) is listed in the legends of Figs. 13, 14 and 15. The last number r is the regression coefficient (if $r = 1$ the regression is perfect).

As expected, Fig. 13 shows that the time to calculate the elements of the impedance matrix(ces) is nearly $\mathcal{O}(N_{\text{Edge}}^2)$ and the use of ACA ($\epsilon_{\text{ACA}} = 10^{-4}, \epsilon_{\text{RACA}} = 10\epsilon_{\text{ACA}} = 10^{-3}$) allows us to reduce this time as $\mathcal{O}(N_{\text{Edge}}^{1.4})$. Theoretically, the complexity can be approximated by $\mathcal{O}(N_{\text{Edge}}^2)(1 - \bar{\tau}_{\text{RACA}})$, where $\bar{\tau}_{\text{RACA}} \in [0.98, 0.99]$ (mean RACA compression ratio, see labeled of Fig. 11 for typical values). The complexity of ACA is $\mathcal{O}(R^2(M + N))$, where R is the matrix rank of size $M \times N$, must be also accounted for. Fig. 13 reveals that the use of PO does not change the time because only $4PN_{\text{Edge}}$

additional elements (in comparison to N_{Edge}^2) are computed. It is important to underline that the times of LU and CBFM should be the same. The explanation is that with CBFM, to compute the P^2 sub-matrices, the associated function (written in C) is called P^2 times from MatLab, whereas only once for LU.

The EFIE-CBFM theoretical complexity (filling time of the impedance matrices not included) is expressed as

$$C_{\text{CBFM}} = C_1 + C_2 + C_3, \tag{24}$$

with

$$\begin{cases} C_1 = P\left[2\mathcal{O}\left(\bar{N}_{\text{Edge,OL}}^3\right) + \bar{N}_{\text{IPW}}\mathcal{O}(\bar{N}_{\text{Edge,OL}}^2)\right] & \text{PBFs computation} \\ C_2 = 2P^2\bar{N}_{\text{IPW,SVD}}\mathcal{O}\left(\bar{N}_{\text{Edge}}^2\right) & \bar{\mathbf{Z}}_R \text{ computation} \\ C_3 = \mathcal{O}\left(N_R^2\right) + \mathcal{O}\left(N_R^3\right) & \text{To solve } \bar{\mathbf{Z}}_R\mathbf{X_R} = \mathbf{b}_R \end{cases}. \tag{25}$$

In C_1, the factor 2 is for the complexities of the SVD and LU decompositions.

Figure 14 shows that the numerical complexity of LU is nearly $\mathcal{O}(N_{\text{Edge}}^{2.8})$ instead of $\mathcal{O}(N_{\text{Edge}}^3)$ for the theoretical one. In Matlab, the function linsolve is applied to solve the linear system and its is well optimized since it is parallelized. The use of CBFM (without parallelization) allows us to reduce the complexity as $\mathcal{O}(N_{\text{Edge}}^{1.8})$ and its hybridization with ACA (in Equation (4), acceleration of the matrix-matrix products because the sub-matrices are compressed) slightly reduces the time.

The use of CBFM-POJ does not require to invert a matrix, that is in Equation (25), $C_1 = P[\mathcal{O}(\bar{N}_{\text{Edge,OL}}^3) + \bar{N}_{\text{IPW}}\mathcal{O}(\bar{N}_{\text{Edge,OL}})]$, whereas CBFM-PO needs this operation. As shown in Section 4.6, to exploit the sparsity of the PO impedance matrix, a basic iterative technique is applied. In addition, the guess is computed by taking the diagonal of the matrix. Numerical tests showed (see Fig. 12) that the method converges rapidly. The theoretical complexity to compute the $2N_{\text{IPW}}$ PBFs of a single block is approximately $\mathcal{O}(4\bar{N}_{\text{Edge,OL}}KN_{\text{IPW}})$, whereas from LU, it is $\mathcal{O}(\bar{N}_{\text{Edge,OL}}^3)$. Therefore, the time saving should be $\bar{N}_{\text{Edge,OL}}^2/(4KN_{\text{IPW}}) \gg 1$. With MatLab, numerical tests (1400 edges; sub-surface of size $(2\lambda)^2$) showed that this ratio is the order of 1. This shows that the function linsolve of MatLab, for which no loop is needed for the calculation of the PBFs, is well optimized (because parallelized) for multiple excitations. When CBFM is hybridized with PO and an iterative solver (like IT or CG), two loops are needed; the first one on the PBFs number and the second one, on the iteration k to obtain the convergence order K. This explains why the complexity (not shown here) is nearly the same between CBFM-LU and CBFM-PO-IT or CBFM-PO-CG.

On the other hand, since the PO impedance matrix is sparse, a specific LU decomposition using this property can be applied. The function lu of the MatLab software has this property. But, for the calculation of the PBFs, it is more relevant to use the MatLab function linsolve which can solve a linear system with multiple excitation vectors but by considering a full matrix (a sparse matrix is not accepted). Comparing lu (with a sparse matrix) and linsolve (the sparse matrix is converted into a full matrix), the computing time is very similar, which means that the computing time to solve a linear system from CBFM-LU and CBFM-PO is nearly the same with MatLab.

The comparison of Fig. 15 with Fig. 14 reveals that the theoretical complexity matches with the numerical one for CBFM. If ACA is hybridized, then the theoretical complexity is underestimated, because the complexity of the ACA algorithm is not accounted for. Theoretically, in Equation (25), the complexity C_1 is multiplied by $1 - \bar{\tau}_{\text{RACA}}$, where $\bar{\tau}_{\text{RACA}} \in [0.98, 0.99]$ (mean RACA compression ratio, see labeled of Fig. 11 for typical values).

Another advantage of CBFM (with or without PO) is that the memory requirement is $P^2\mathcal{O}(\bar{N}_{\text{IPW,SVD}}^2)$, whereas for a conventional MoM, it is $P^2\mathcal{O}(\bar{N}_{\text{Edge}}^2)$. In addition, once the characteristic matrix $\bar{\mathbf{Z}}^{\text{R}}$ is calculated and stored, multiple excitations can simultaneously be handled with linsolve. It is also possible with a conventional MoM, but the entire impedance matrix must be stored, which is impossible for huge problems.

With CBFM, the comparison of Fig. 13 with Fig. 14 shows that the time allocated to compute the sub-matrices is larger than that to solve the linear system. Another advantage of a domain decomposition method is its ability to be parallelized. This procedure will allow us to reduce the computing time of the first (calculation of the self-impedance sub-matrices and the PBFs) and second

(computation of the characteristic matrix) stages of CBFM. With respect to the CBFM stages, a detailed analysis of the complexity is addressed in [20].

5. CONCLUSION

This paper proved that the CBFM is a very efficient method to calculate the RCS from a large object, for which multiple refection occurs. In addition, to accelerate the calculation of the PBFs, the PO approximation with single refection is applied. The PO impedance matrix needs to be derived from the EFIE to avoid to apply the MFIE. To our knowledge, it is the first time that this derivation is addressed. Its numerical computation requires to nearly calculate $4N_{\text{Edge}}$ elements instead of N_{Edge}^2. Numerical tests on different targets showed that EFIE-CBFM-PO match very well with EFIE-CBFM-LU and the conventional MoM. In addition, a simple iterative algorihtm is addressed to accelerate the PBFs calculation with PO. The fact to invert the matrix allows us to have a robuster PO versus the surface curvature, unlike POJ.

REFERENCES

1. Gibson, W. C., *The Method of Moments in Electromagnetics*, Chapman and Hall/CRC, London, 2008.
2. Quarteroni, A., R. Sacco, and F. Sameri, *Méthodes Numériques: Algortihmes, Analyse et Applications*, Springer-Verlag, New-York, 2007.
3. Coifman, R., V. Rokhlin, and S. Wandzura, "The fast multipole method for the wave equation: A pedestrian prescription," *IEEE Antennas and Propagation Magazine*, Vol. 35, No. 3, 7–12, 1993.
4. Song, J. M., C. C. Lu, and W. C. Chew, "Multilevel fast multipole algorithm for electromagnetic scattering by large complex objects," *IEEE Transactions on Antennas and Propagation*, Vol. 45, No. 10, 488–1493, 1997.
5. Jandhyala, V., E. Michielssen, B. Shanker, and W. C. Chew, "A combined steepest descent-fast multipole algorithm for the fast analysis of threedimensional scattering by rough surfaces," *IEEE Transactions on Geoscience and Remote Sensing*, Vol. 36, No. 5, 738–748, 1998.
6. Bleszynski, E., M. Bleszynski, and T. Jaroszewicz, "AIM: Adaptive integral method for solving large-scale electromagnetic scattering and radiation problems," *Radio Science*, Vol. 31, No. 5, 1225–1251, 1996.
7. Bagci, H., A. E. Yilmaz, J.-M. Jin, and E. Michielssen, *Modeling and Computations in Electromagnetics — Chapter 3: Time Domain Adaptive Integral Method for Surface Integral Equations*, H. Ammari, Ed., Springer, Berlin, 2000.
8. Ewe, W.-B., L.-W. Li, and M.-S. Leong, "Solving mixed dielectric/conducting scattering problem using adaptive integral method," *Progress In Electromagnetics Research*, Vol. 163, 143–163, 2004.
9. Colliander, A. and P. Yla-Oijala, "Electromagnetic scattering from rough surface using single integral equation and adaptive integral method," *IEEE Transactions on Antennas and Propagation*, Vol. 55, No. 12, 3639–3646, 2007.
10. Wang, X., S.-X. Gong, J. Ling, and X.-M. Wang, "Interpolation scheme based on adaptive integral method for solving electrically large radiation problem by surface/surface configuration," *Progress In Electromagnetics Research M*, Vol. 11, 203–211, 2010.
11. Zhou, L., L. Tsang, V. Jandhyala, Q. Li, and C. H. Chan, "Emissivity simulations in passive microwave remote sensing with 3-D numerical solutions of Maxwell equations," *IEEE Transactions on Geoscience and Remote Sensing*, Vol. 42, No. 8, 1739–1748, 2004.
12. Huang, S. W., G. H. Zhang, M. Y. Xia, and C. H. Chan, "Numerical analysis of scattering by dielectric random rough surfaces using modified SMCG scheme and curvilinear RWG basis functions," *IEEE Transactions on Antennas and Propagation*, Vol. 57, No. 10, 3392–3397, 2009.
13. Liao, T.-H., L. Tsang, S. Huang, N. Niamsuwan, S. Jaruwatanadilok, S.-B. Kim, H. Ren, and K.-L. Chen, "Copolarized and cross-polarized backscattering from random rough soil surfaces from L-

band to Ku-band using numerical solutions of Maxwell's equations with near-field precondition," *IEEE Transactions on Geoscience and Remote Sensing*, Vol. 54, No. 2, 651–662, 2016.

14. Qiao, T., L. Tsang, D. Vandemark, S. H. Yueh, T.-H. Liao, F. Nouguier, and B. Chapron, "Sea surface radar scattering at L-band based on numerical solution of Maxwell's equations in 3-D (NMM3D)," *IEEE Transactions on Geoscience and Remote Sensing*, Vol. 56, No. 6, 3137–3147, 2018.
15. Bourlier, C., "Scattering from quasi-planar and moderate rough surfaces: Efficient method to fill the EFIE-Galerkin MoM impedance matrix and to solve the linear system," *IEEE Transactions on Antennas and Propagation*, Vol. 69, No. 9, 5761–5770, Jan. 2021.
16. Prakash, V. S. and R. Mitra, "Characteristic basis function method: A new technique for efficient solution of method of moments matrix equations," *Microwave Optical Technology Letter*, Vol. 26, No. 2, 95–100, 2003.
17. Bourlier, C., N. Pinel, and G. Kubické, "Propagation-inside-layer-expansion method combined with physical optics for scattering by coated cylinders, a rough layer, and an object below a rough surface," *Journal of the Optical Society of America A*, Vol. 30, No. 9, 1727–1737, 2013.
18. Bourlier, C. S. Bellez, and G. Kubické, "Sub-domain decomposition iterative method combined with ACA: An efficient technique for the scattering from a large highly conducting rough sea surface," *IEEE Transactions on Antennas and Propagation*, Vol. 63, No. 2, 659–666, 2015.
19. Bellez, S., C. Bourlier, and G. Kubické, "An efficient PILE algorithm for solving the scattering from three-dimensional (3-D) nested homogeneous dielectric bodies," *Journal of the Optical Society of America A*, Vol. 32, No. 3, 392–401, 2015.
20. Bourlier, C., Y. Arencibia Noa, and G. Kubické, "Two domain decomposition methods, SDIM and CBFM, for the scattering from a two-dimensional perfectly-conducting rough surface: Comparison and parametric study," *Journal of the Optical Society of America A*, Vol. 37, No. 9, 1512–1525, 2020.
21. Yagbasan, A., C. A. Tunc, V. B. Erturk, A. Altintas, and R. Mitra, "Characteristic basis function method for solving electromagnetic scattering problems over rough terrain profiles," *IEEE Transactions on Antennas and Propagation*, Vol. 58, No. 5, 1579–1589, 2010.
22. Garcia, E., C. Delgado, L. Plata Lozano, I. Gonzalez-Diego, and M. Felipe Catedra, "An efficient hybrid-ccheme combining the characteristic basis function method and the multilevel fast multipole algorithm for solving bistatic RCS and radiation problems," *Progress In Electromagnetics Research B*, Vol. 34, 327–343, 2011.
23. Li, C. and R. Mittra, "Characteristic basis function method for fast analysis of 3-D scattering from objects buried under rough surfaces," *IEEE Transactions on Geoscience and Remote Sensing*, Vol. 57, No. 8, 5252–5265, 2019.
24. Xia, C., W. You, and Y. Sun, "Fast calculation of monostatic radar cross section of conducting targets using hierarchical characteristic basis function method and singular value decomposition," *Progress In Electromagnetics Research Letters*, Vol. 81, 133–139, 2019.
25. Bourlier, C., "Rough layer scattering filled by elliptical cylinders from the method of moments combined with the characteristic basis function method and the Kirchoff approximation," *Journal of the Optical Society of America A*, Vol. 38, No. 10, 1581–1593, 2021.
26. Pouliguen, P., R. Hemon, C. Bourlier, J. F. Damiens, and J. Saillard, "Analytical formulae for radar cross section of at plates in near field and normal incidence," *Progress In Electromagnetics Research*, Vol. 9, 263–279, 2008.
27. Vallecchi, A., "Physical optics curved-boundary dielectric plate scattering formulas for an accurate and efficient electromagnetic characterization of a class of natural targets," *IEEE Transactions on Geoscience and Remote Sensing*, Vol. 46, No. 6, 1657–1666, 2008.
28. Bourlier, C. and P. P. Pouliguen, "Useful analytical formulae for nearfield monostatic radar cross section under the physical optics: Far-field criterion," *IEEE Transactions on Antennas and Propagation*, Vol. 57, No. 1, 205–214, 2009.
29. Corbel, C., C. Bourlier, N. Pinel, and J. Chauveau, "Rough surface RCS measurements and simulations using the physical optics approximation," *IEEE Transactions on Antennas and*

Propagation, Vol. 61, No. 10, 5155–5165, 2013.

30. Kubické, G., C. Bourlier, M. Delahaye, C. Corbel, and N. Pinel, "Bridging the gap between the babinet principle and the physical optics approximation: Vectorial problem," *Radio Science*, Vol. 48, No. 5, 573–581, 2013.
31. Karaca, S. and A. A. Ergin, "Closed-form time domain PO expressions of the electric field scattered from PEC objects illuminated by an electric dipole," *IEEE Transactions on Antennas and Propagation*, Vol. 63, No. 10, 4477–4485, 2015.
32. Ludwig, A., "Computation of radiation patterns involving numerical double integration," *IEEE Transactions on Antennas and Propagation*, Vol. 16, No. 6, 767–769, 1968.
33. Corucci, L., E. Giusti, M. Martorella, and F. Berizzi, "Near field physical optics modelling for concealed weapon detection," *IEEE Transactions on Antennas and Propagation*, Vol. 60, No. 12, 6052–6057, 2012.
34. An, Y., D. Wang, and R. Chen, "Improved multilevel physical optics algorithm for fast computation of monostatic radar cross section," *IET Microw., Antennas Propag.*, Vol. 8, No. 2, 93–98, 2014.
35. Zhang, J., B. Xu, and T. J. Cui, "An alternative treatment of saddle stationary phase points in physical optics for smooth surfaces," *IEEE Transactions on Antennas and Propagation*, Vol. 62, No. 2, 986–991, 2014.
36. Boag, A., "A Fast Physical Optics (FPO) algorithm for high frequency scattering," *IEEE Transactions on Antennas and Propagation*, Vol. 52, No. 1, 197–204, 2004.
37. Zhang, J., W. M. Yu, X. Y. Zhou, and T. J. Cui, "Efficient evaluation of the physical-optics integrals for conducting surfaces using the uniform stationary phase method," *IEEE Transactions on Antennas and Propagation*, Vol. 60, No. 5, 2398–2408, 2012.
38. De Adana, F. S., S. Nieves, E. Garcia, I. Gonzalez, O. Gutierrez, and M. F. Catedra, "Calculation of the RCS from the double reflection between planar facets and curved surfaces," *IEEE Transactions on Antennas and Propagation*, Vol. 51, No. 9, 2509–2512, 2003.
39. Catedra, M. F., C. Delgado, S. Luceri, O. G. Blanco, and F. S. de Adana, "Physical optics analysis of multiple interactions in large scatters using current modes," *IEEE Transactions on Antennas and Propagation*, Vol. 54, No. 3, 985–994, 2006.
40. Delgado, C., J. M. Gomez, and M. F. Catedra, "Analytical field calculation involving current modes and quadratic phase expressions," *IEEE Transactions on Antennas and Propagation*, Vol. 55, No. 1, 233–240, 2007.
41. Kubické, G., C. Bourlier, and J. Saillard, "Polarimetric bistatic signature of a faceted octahedron in high-frequency domain," *Progress In Electromagnetics Research*, Vol. 71, 173–209, 2007.
42. Kubické, G., C. Bourlier, and J. Saillard, "High-frequency bistatic scattering by depolarizing, nearly omnidirectional reflectors: Higher order polyhedral reflectors," *IEEE Transactions on Antennas and Propagation*, Vol. 56, No. 9, 3029–3035, 2008.
43. Jackson, J. A., "Analytic physical optics solution for bistatic, 3D scattering from a dihedral corner reflector," *IEEE Transactions on Antennas and Propagation*, Vol. 60, No. 3, 1486–1495, 2012.
44. Roudstein, M., Y. Brick, and A. Boag, "Multilevel physical optics algorithm for near-field double-bounce scattering," *IEEE Transactions on Antennas and Propagation*, Vol. 63, No. 11, 5015–5025, 2015.
45. Bourlier, C., G. Kubické, and P. Pouliguen, "Accelerated computation of the physical optics approximation for near-field single- and double-bounces backscattering," *IEEE Transactions on Antennas and Propagation*, Vol. 67, No. 12, 7518–7527, 2019.
46. Obelleiro-Basteiro, F., J. L. Rodriguez, and R. J. Burkholder, "An iterative physical optics approach for analyzing the electromagnetic scattering by large open-ended cavities," *IEEE Transactions on Antennas and Propagation*, Vol. 43, No. 4, 356–361, 1995.
47. Obelleiro, F., J. Campos-Nino, J. L. Rodriguez, and A. G. Pino, "A segmented approach for computing the electromagnetic scattering of large and deep cavities," *Progress In Electromagnetics Research*, Vol. 19, 129–145, 1998.
48. Anastassiu, H. T., "A review of electromagnetic scattering analysis for inlets, cavities and open

products," *IEEE Antennas and Propagation Magazine*, Vol. 45, No. 6, 27–40, 2003.

49. Bourlier, C., H. He, J. Chauveau, R. Hémon, and P. Pouliguen, "RCS of large bent waveguide from a modal analysis combined with the Kirchoff approximation," *Progress In Electromagnetics Research*, Vol. 88, 1–38, 2008.
50. R. J. Burkholder, C. Tokgoz, C. J. Reddy, and W. O. Coburn, "Iterative physical optics for radar scattering predictions," *J.-Appl. Comput. Electromagn. Soc.*, Vol. 24, No. 2, 241–258, 2009.
51. Thomet, A., G. Kubické, C. Bourlier, and P. Pouliguen, "Low computational cost method for scattering of large cavities based on ACA compression of Iterative Physical Optics," *Int. Conf. Electromagn. Adv. Appl. (ICEAA)*, 207–210, Sep. 2015.
52. Hémon, R., P. Pouliguen, J. Saillard, and J. F. Damiens, "Implementation of the equivalent currents method in the IPO method," *2008 IEEE Antennas and Propagation Society International Symposium*, San Diego, CA, Jul. 2008.
53. Michaeli, A., "Equivalent edge currents for arbitrary aspects of observations," *IEEE Transactions on Antennas and Propagation*, Vol. 23, No. 3, 252–258, 1984.
54. Knott, E. F., "The relationship between Mitzner's ILDC and Michaeli's equivalent currents," *IEEE Transactions on Antennas and Propagation*, Vol. 33, No. 1, 112–114, 1985.
55. Jakobus, U. and M. Landstorfer, "Improved PO-MM hybrid formulation for scattering from three-dimensional perfectly conducting bodies of arbitrary shape," *IEEE Transactions on Antennas and Propagation*, Vol. 43, No. 2, 162–169, 1995.
56. Bebendorf, M. and S. Rjasanow, "Adaptive low-rank approximation of collocation matrices," *Computing*, Vol. 701, No. 1, 1–24, 2003.
57. Zhao, K., M. N. Vouvakis, and J.-F. Lee, "The adaptive cross approximation algorithm for accelerated method of moments computations of EMC problems," *IEEE Transactions on Electromagnetic Compatibility*, Vol. 47, No. 4, 763–773, 2005.
58. Rao, S., D. Wilton, and A. Glisson, "Electromagnetic scattering by surfaces of arbitrary shape," *IEEE Transactions on Antennas and Propagation*, Vol. 30, No. 409-18, 1982.
59. Lucente, E., A. Monorchio, and R. Mittra, "An iteration-free MoM approach based on excitation independent characteristic basis functions for solving large multiscale electromagnetic scattering problems," *IEEE Transactions on Antennas and Propagation*, Vol. 56, No. 4, 999–1007, 2008.
60. Tsang, L., J. A. Kong, and K.-H. Ding, *Scattering of Electromagnetic Waves, Theories and Applications, W. S. in Remote Sensing*, John Wiley & Sons, Inc., 2000.